Journal of Materials Chemistry A

Accepted Manuscript

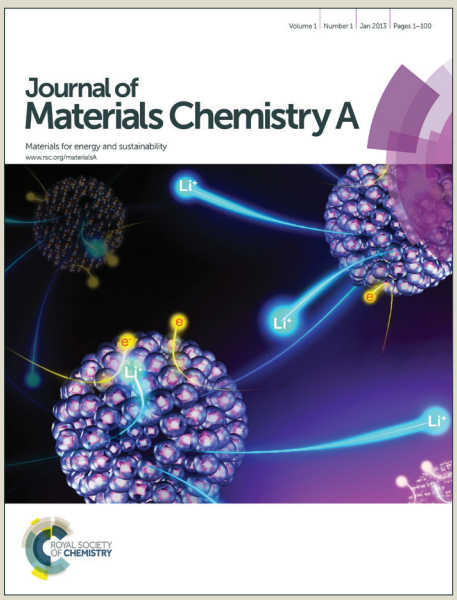

ROYAL SOCIETY OF CHEMISTRY

www.rsc.org/materialsA

Journal of
Materials Chemistry A

Dynamic Article Links ►

Cite this: DOI: 10.1039/c0xx00000x

www.rsc.org/xxxxxx

Full paper

In-situ synthesis of C-doped $(BiO)_2CO_3$ hierarchical self-assembly effectively promoting visible light photocatalysis

Ting Xiong [a], Hongwei Huang [b], Yanjuan Sun [a], Fan Dong [a,*]

Abstract: Development of high-performance visible light photocatalysts is the key to environmental and energetic application of photocatalysis technology. By combination of doping and structural optimization, semiconductors with wide band gap could transform into highly active visible light photocatalysts. In this work, C-doped $(BiO)_2CO_3$ microspheres hierarchically constructed by self-assembled nanosheets were prepared via a facile hydrothermal method applying glucose as carbon source for the first time. The incorporation of external C element into the crystal structure of $(BiO)_2CO_3$ could narrow the band gap by down-shifting the conduction band, and meantime generate some localized states above the valence band edge. The C-doped $(BiO)_2CO_3$ hierarchical self-assembly exhibited highly enhanced and stable photocatalytic activity for NO removal under visible light illumination, far exceeding those of undoped $(BiO)_2CO_3$, C-doped TiO_2 and N-doped $(BiO)_2CO_3$. The improved photocatalytic activity could be attributed to the increased visible light absorption, improved charge separation and transfer as well as the special hierarchical structure. The C-doped $(BiO)_2CO_3$ microspheres also generated enhanced visible light induced photocurrent density. There exists an optical amount of C element introduced into the crystal structure. In addition, the growth mechanism of C-doped $(BiO)_2CO_3$ hierarchical microspheres has been proposed. By using other carbohydrates like maltose, fructose, sucrose and starch as carbon doping source, C-doped $(BiO)_2CO_3$ can also be synthesized, which indicates that carbohydrate is a general type of carbon doping source. This work could provide a one-step and general method to fabricate high-active C-doped $(BiO)_2CO_3$ photocatalysts, which simultaneously shed new insight into the enhancement of visible photocatalysis by combination of carbon doping and structural optimization.

1. Introduction

To mitigate the environmental and energy issues, semiconductor photocatalysis as a promising technology which can utilize the sustainable solar energy or artificial indoor light to remove hazardous substances or split water to generate hydrogen fuel have been extensively investigated.[1-5]

Many semiconductor photocatalysts suffer from deficient absorption of sunlight resulting from the large bandgap, which limits their applications.[6-8] Hence, considerable effort has been expended to narrow the bandgap to coincide with the solar spectrum, which is an active research area with strategies mainly based on doping metals and nonmetals.[9-13] Among various modification methods, carbon doping has shown great potential in improving the visible photocatalytic activity of wide bandgap semiconductors. The incorporation of carbon element into the crystal structure of semiconductors can either narrow the bandgap via tailoring the composition of the band or

[a] Chongqing Key Laboratory of Catalysis and Functional Organic Molecules, College of Environmental and Biological Engineering, Chongqing Technology and Business University, Chongqing, 400067, China.
[b] Beijing Key Laboratory of Nonmetallic Minerals and Material Utilization of Solid Wastes, China University of Geosciences, Beijing 100083, China.
*To whom correspondence should be addressed.
E-mail: dfctbu@126.com (Fan Dong). Tel.: +86-23-62769785-605; Fax: +86-23-62769785-605.
Electronic supplementary information (ESI) available: Detailed and additional figures as noted in the text. See DOI: 10.1039/b000000x

generate isolated C 2p states in the band gap, and then increase visible light absorption.[11,14-17]

Recently, interests in the synthesis of semiconductor materials with controllable shapes have dramatically increased because of their shape dependent physical, chemical, electronic, optical, and catalytic properties.[18-21] Compared with the low-dimensional structure, 3D hierarchical structure materials showed excellent photocatalytic performances in H_2 production, pollutants removal, and CO_2 reduction benefiting from the large surface areas, special pore structure, efficient light harvesting and charge separation. As a consequence, 3D hierarchical structure semiconductors have been widely fabricated and applied in photocatalysis.[22-25] Most recently, fabrication of 3D hierarchical structures is reported to be an effective way to boost the visible light absorption of wide bandgap semiconductors through the reflection and scattering effects.[26,27]

$(BiO)_2CO_3$, with an orthorhombic crystal structure constructed by $(BiO)_2^{2+}$ layers sandwiched between two sheets of CO_3^{2-} (Fig. S1), has been explored and applied in antibacterial,[28] sensing,[29] super capacitor[30] and photocatalysis.[31-33] As the photoresponse of pure $(BiO)_2CO_3$ is mainly in the ultraviolet region, some attempts have been made to improve the visible photocatalytic activity of $(BiO)_2CO_3$, including nitrogen doping,[34,35] noble deposition[30,36] and heterojunction structure formation.[37-41] However, the photocatalytic activity of $(BiO)_2CO_3$ is far from high efficiency for practical applications and it is necessary to explore other strategies to enhance the photocatalytic efficiency.

Inspired by the widely investigated strategies involved with carbon doping and structural optimization, we believe that it is significant to combine the two strategies on one attractive material $(BiO)_2CO_3$ and fabricate C-doped $(BiO)_2CO_3$ with 3D hierarchical microspheres structure, which could make $(BiO)_2CO_3$ highly active under visible light. Herein, a simple one-pot hydrothermal process has been developed to synthesize C-doped $(BiO)_2CO_3$ hierarchical self-assembly using glucose as carbon source. The experimental results indicated that the C-doped $(BiO)_2CO_3$ showed narrowed bandgap with an increase in the doped carbon content in comparison with bare $(BiO)_2CO_3$. The bandgap was narrowed by down-shifting the conduction band, accompanying with the generation of some localized states above the valence band edge. The increased visible light absorption and efficient separation of electron−hole pairs benefiting from the doped carbon and special hierarchical structure resulted in the enhanced visible photocatalytic activity of C-doped $(BiO)_2CO_3$. The as-prepared C-doped $(BiO)_2CO_3$ showed highly enhanced visible light photocatalytic activity towards the removal of NO in comparison with the undoped $(BiO)_2CO_3$ and some other well-known photocatalysts such as C-doped TiO_2 and N-doped $(BiO)_2CO_3$. Moreover, the admirable photocatalytic activity of the as-prepared C-doped $(BiO)_2CO_3$ photocatalysts are stable and reproducible. The growth mechanism of the C-doped $(BiO)_2CO_3$ microspheres assembled by nanosheets was studied based on time-dependent observation. The effect of different carbon source on fabricating C-doped $(BiO)_2CO_3$ microspheres was also investigated. It was found that carbohydrate could act as a general carbon doping source.

2. Experimental section

2.1 Synthesis of C-doped $(BiO)_2CO_3$ hierarchical self-assembly

All chemicals used in this study were analytical grade (Sigma Aldrich) and were used without further purification. In a typical synthesis, sodium carbonate (0.46 g) was dissolved in 72 mL of water in a 100 mL autoclave Teflon vessel with stirring for 10 min. Then bismuth citrate (1.60 g) was added into the above aqueous solution and stirred for 30 min. After this, appropriate amounts of glucose was added into the above suspension and stirred for 10 min. The resulting aqueous precursor suspension was then hydrothermally treated at 180 ^oC for 24 h. After the reaction, the sample obtained was filtered, washed with water and ethanol for three times and dried at 70 ^oC for 12 h to get final products without further treatment. According to the content of glucose (0.0580 g, 0.1160 g, 0.20 g), the samples were labeled as CBOC-L, CBOC-M and CBOC-H, respectively. In addition, $(BiO)_2CO_3$ was synthesized without adding glucose and was denoted as BOC.

2.2 Characterization

The crystal phases of the sample were analyzed by X-ray diffraction (XRD) with Cu Kα radiation (model D/max RA, Rigaku Co., Japan). Fourier transform infrared (FTIR) spectra were recorded on a Nicolet Nexus spectrometer on samples embedded in KBr pellets. Scanning electron microscopy (SEM; model JSM-6490, JEOL, Japan) was used to characterize the morphology of the obtained products. The morphology and structure of the samples were examined by transmission electron microscopy (TEM; JEM-2010, Japan). X-ray photoelectron spectroscopy (XPS) with Al Kα X-rays (hm = 1486.6 eV) radiation operated at 150 W (Thermo ESCALAB 250, USA) was used to investigate the surface properties. The UV-vis diffuse-reflectance spectrometry (DRS) spectra were obtained for the dry-pressed disk samples using a Scan UV-vis spectrophotometer (TU-1901, China) equipped with an integrating sphere assembly, using 100% $BaSO_4$ as the reflectance sample. The photoluminescence spectra (PL) for the samples were obtained using a fluorescence spectrophotometer (FS-2500, Japan) with an Xe lamp with optical filter as the excitation source.Nitrogen adsorption–desorption isotherms were obtained on a nitrogen adsorption apparatus (ASAP 2020, USA). All the samples were degassed at 150 ^oC prior to measurements. The

photocurrent response and electrochemical impedance spectra measurements were performed in three-electrode quartz cells with a 0.1 M Na_2SO_4 electrolyte solution. Platinum wire was used as the counter electrode, and saturated calomel electrodes were used as the reference electrodes. $(BiO)_2CO_3$ and C-doped $(BiO)_2CO_3$ film electrodes on ITO served as the working electrode. The photoelectrochemical experiment results were recorded using an electrochemical system (CHI-660B, China). All the photoelectrochemical measurements are performed under visible light of a 500 W Xe lamp coupling with 420 nm cutoff filters, and the average light power is 45 mW/cm^2.

2.3 Evaluation of photocatalytic activity

The as-prepared samples was applied for photocatalytic activity removal of NO at ppb level in a continuous flow reactor under visible light irradiation. The reactor was 4.5 L (30 cm × 15 cm × 10 cm), made of polymeric glass, and covered with Saint-Glass. A commercial tungsten halogen lamp (150 W) was vertically placed 20 cm above the reactor, and the average light intensity was 0.16 W cm^{-2}. A UV cut-off filter (420 nm) was applied to remove UV light for the test of photocatalytic activity in visible light region (420-780nm). The as-prepared sample (0.20 g) was dispersed in distilled water (50 ml) in a beaker via ultrasonic treatment for 10 min and then coated onto two glass dishes (12.0 cm in diameter). The coated dishes were pretreated at 70 ℃ to remove water in the suspension and were placed at the center of the reactor. The NO gas was acquired from a compressed gas cylinder at a concentration of 100 ppm of NO (N_2 balance). The initial concentration of NO was diluted to about 600 ppb. The flow rates of the air stream and NO were controlled at 2.4 L/min and 15 mL/min, respectively. The two gas streams were then premixed in a three-way valve. The relative humidity is controlled at 50% in the air stream. When the adsorption-desorption equilibrium was achieved, the lamp was turned on. The concentration of NO was measured every one min by using an NOx analyzer (Thermo Scientific, 42i-TL), which also monitored the concentration of NO_2 and NO_x (NO_x represents NO + NO_2). The removal ratio (η) of NO was calculated using η (%) = $(1 - C/C_0) \times 100\%$, where C is the outlet concentration of NO after reaction for time t, and C_0 represents the inlet concentration after achieving adsorption-desorption equilibrium.

3. Results and discussion

3.1 Phase Structure and Surface Properties.

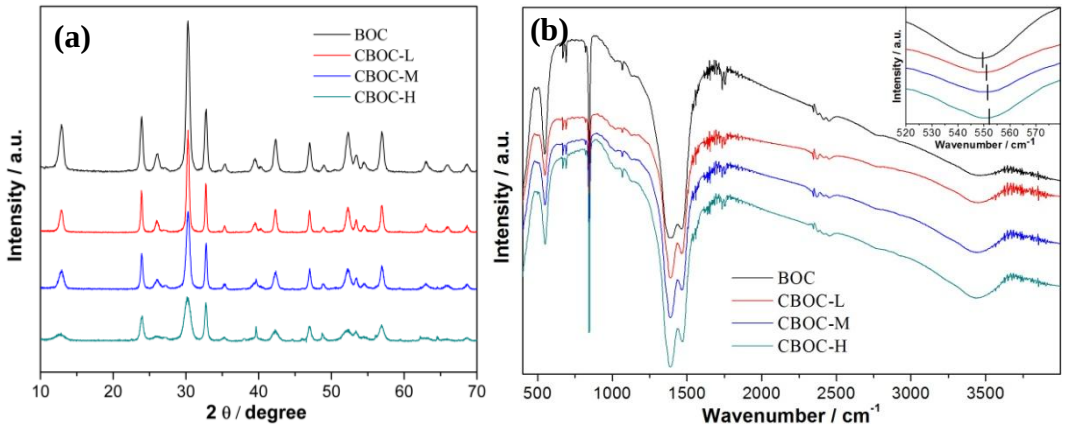

Fig. 1 XRD patterns (a) and FT-IR spectra (b) of the as-prepared samples.

Fig. 1a shows the XRD patterns of the un-doped $(BiO)_2CO_3$ and C-doped $(BiO)_2CO_3$. The XRD diffraction patterns of the C-doped $(BiO)_2CO_3$ are similar to that of un-doped $(BiO)_2CO_3$, which can be indexed to the $(BiO)_2CO_3$ (JCPDS-ICDD card no. 25-1464) with no impurity peaks detected. With the increase in glucose content, the peak intensity decreases, suggesting the level of carbon doping has a significant effect on the crystal growth. In Fig. 1b, the internal vibrations of the "free" CO_3^{2-} ion (point group symmetry D_{3h}),[42] that is, symmetric stretching mode v_1 (1064 cm^{-1}), the anti-symmetric vibration v_3 (1469 and 1391 cm^{-1}), the out-of-plane bending mode v_2 (842 and 818 cm^{-1}), the in-plane deformation v_4 (690 and 671 cm^{-1}), and v_1+v_4 (1750 and 1735 cm^{-1}), can be observed for the four samples. Besides, the vibration peak at around 550 cm^{-1} belonging to the Bi-O bond can be detected, and a slight red-shift can be seen with increased glucose content (inset). This can be caused by the doped carbon atoms which substitute the oxygen atoms bonding to Bi atoms. Since the stretching modes of CO_3^{2-} are similar in the un-doped $(BiO)_2CO_3$ and C-doped $(BiO)_2CO_3$, suggesting that C was not incorporated into the CO_3^{2-} group. Alternatively, the carbon atoms can immerge into the $(BiO)_2^{2+}$ group. The broad peak at 1500–1600 cm^{-1} corresponding to the characteristic stretching vibrations of surface hydroxyl groups are broader and stronger in the C-doped $(BiO)_2CO_3$ than that of un-doped $(BiO)_2CO_3$. The surface hydroxyl groups can trap the holes generated

under irradiation to form hydroxyl radicals which can initiate the photocatalytic reaction and suppress electron-hole recombination.[15]

3.2 Morphology and Structure.

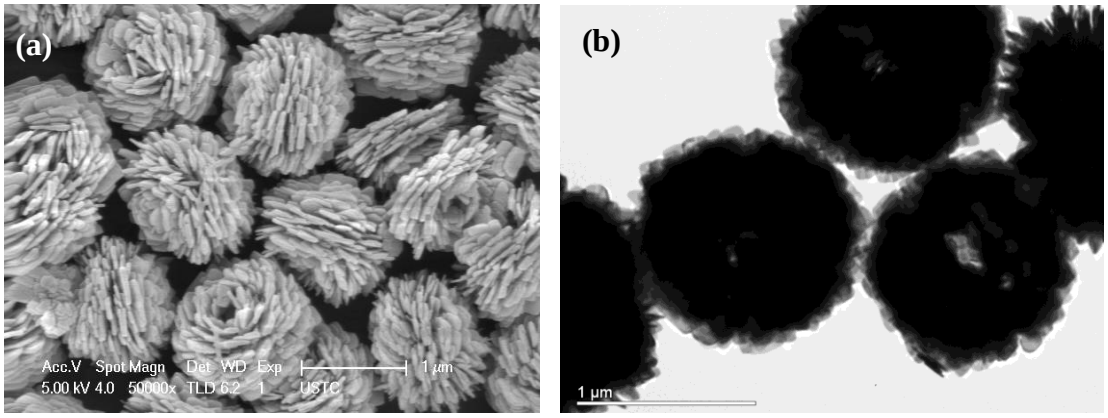

Fig. 2 SEM (a) and TEM (b) images of the as-prepared BOC sample.

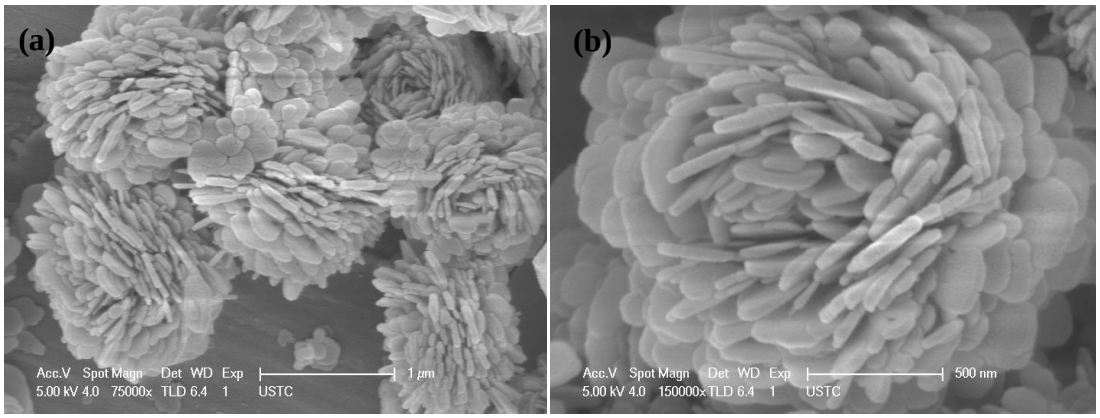

Fig. 3 SEM (a, b) images of the as-prepared CBOC-L sample.

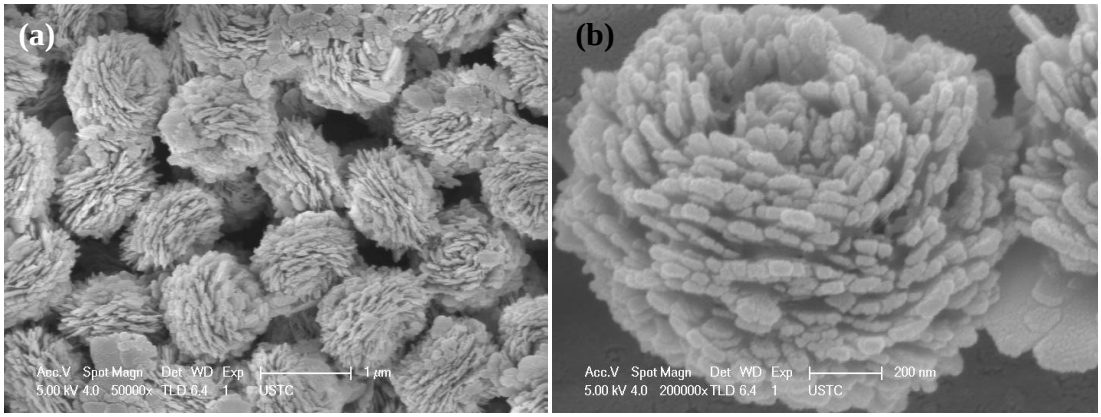

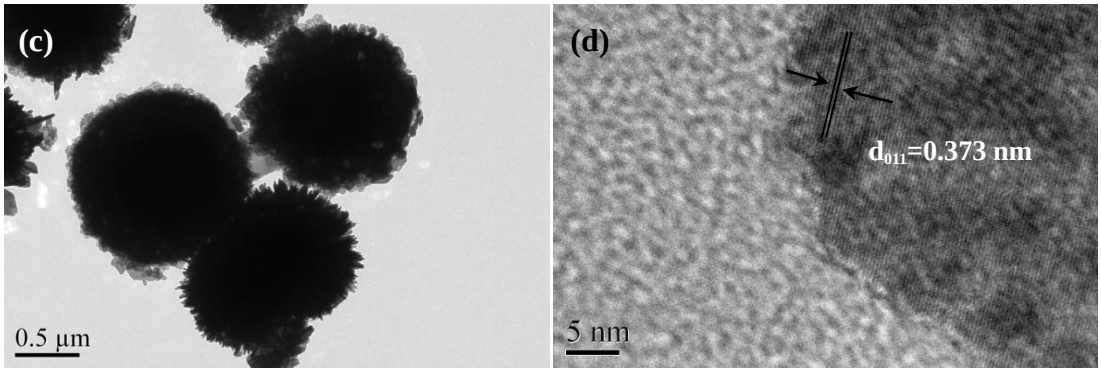

Fig. 4 SEM (a, b) and TEM (c, d) images of the as-prepared CBOC-M sample.

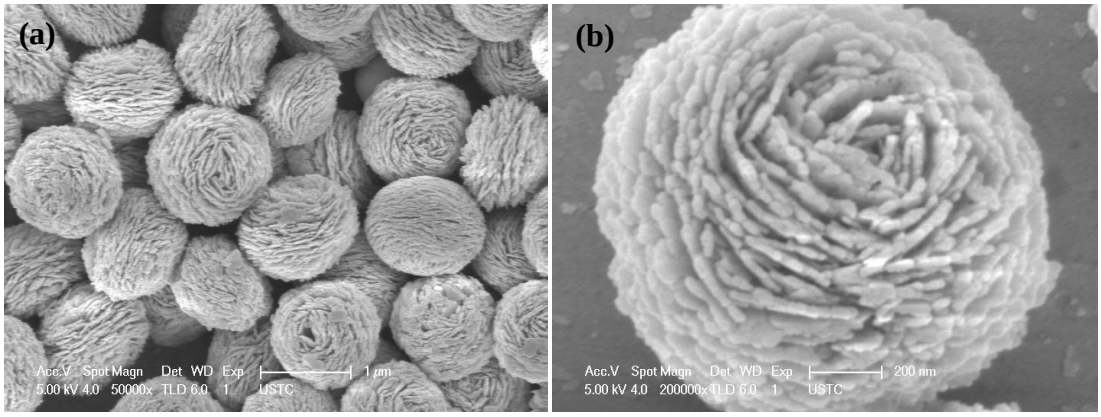

Fig. 5 SEM (a, b) images of the as-prepared CBOC-H sample.

The morphology and structure of the obtained samples were investigated by SEM and TEM as shown in Fig. 2-5. Fig. 2a displays the SEM images of BOC, in which the BOC sample with average size of 1.3 μm are consisted of self-assembled nanosheets. As revealed by the previous research,[43] The internal layered structure of $(BiO)_2CO_3$ would guide the lower growth rate along certain axis to form 2D nanosheets. And, the auto self-assembly of these nanosheets leads to the formation of $(BiO)_2CO_3$ hierarchical microspheres. Also, the aggregation of the self-assembled nanosheets endows the microspheres with mesopores, which is favorable for the light harvesting and reactants transport. TEM image in Fig. 2b further demonstrates its microspheres structure, and the microsphere is hollow in the center. However, the C-doped $(BiO)_2CO_3$ exhibits a slightly different morphology with BOC.

Fig. 3a and b display the SEM images of the CBOC-L sample. CBOC-L mainly presented porous microspheres structure with size in ca. 1.7 μm. Besides, some unassembled nanosheets around the microspheres can be observed. The SEM images of CBOC-M sample are shown in Fig. 4a and b. Similarly, microspheres with size of ~1.4 μm together with some unassembled nanosheets can be observed. Meantime, the nanosheets become small, which reflects that introduction of external C element affects the growth of the nanosheets, in agreement with the XRD analysis. The TEM image shown in Fig. 4c confirms its microspheres morphology, and notably, the center of the microspheres are solid, which differs from the BOC samples, confirming that these nanosheets are much more densely arranged than BOC. The observed spacing between the lattice planes of a single nanosheet in CBOC-M from Fig. 4d is estimated to be 0.373 nm, in coincidence with the space distance of (011) plane. Fig. 5a and b displays the SEM images of CBOC-H, which shows a uniform diameter of 1.3 μm. The nanosheets are much more densely arranged to form the microspheres structure, and few small nanosheets still can be found. These results mean that carbon doping influences the growth of nanosheets but has a minor effect on the self-assembly of the nanosheets to form microspheres although some unassembled nanosheets can be observed.

Fig. S2a shows the nitrogen adsorption-desorption isotherm curves of undoped $(BiO)_2CO_3$ and C-doped $(BiO)_2CO_3$. The samples exhibit a type IV adsorption isotherm with an H3 hysteresis loop, which are typically characteristic of mesoporous structure,[44] consistent with the SEM results. In fact, the mesopore stems from the aggregation of nanosheets. The pore size distribution curve is quite broad (from 2 to 100 nm) with a maximum pore diameter of around 22 to 31 nm, which further proves that hierarchical microspheres have a mesoporous structure (Fig. S2b). Such organized porous structures are very useful in photocatalysis because they possess efficient transport pathways to reactants and products.[20] The BET surface area, pore size, and volume of the four samples are also shown in Table 1. It can be seen that the BET surface areas (S_{BET}) and pore volumes of C-doped $(BiO)_2CO_3$ are close to that of the undoped $(BiO)_2CO_3$.

3.3 Chemical Composition and Band Structure.

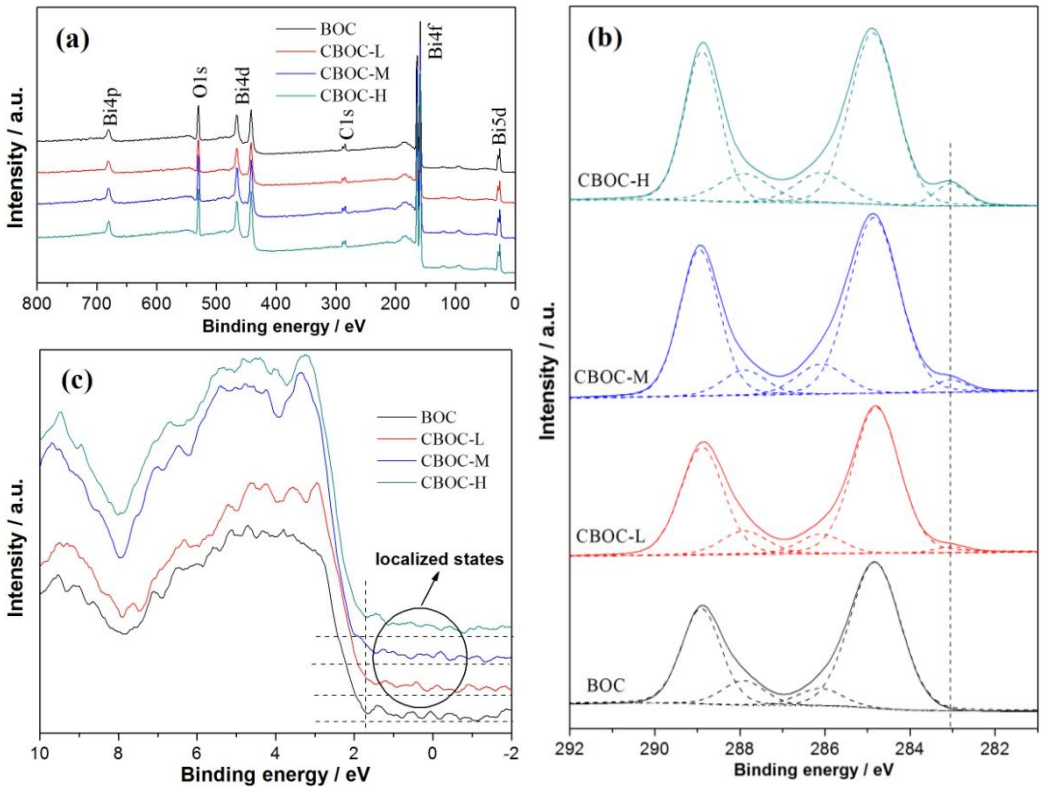

Fig. 6 XPS spectra of the undoped $(BiO)_2CO_3$ and C-doped $(BiO)_2CO_3$, (a) survey, (b) C1s and (c) valence band.

To investigate the chemical states of related elements and total density of states distribution (DOS) of the valence band in the as-prepared samples, X-ray photoelectron spectroscopy were performed as shown in Fig. 6. The survey spectra in Fig. 6a imply the presence of Bi, O and C elements in the four samples without other element detected. Fig. 6b presents the C1s spectra with a broad energy range from 292 to 281 eV of the as-prepared samples. The peaks at 284.8, 286.1 and 287.9 eV can be assigned to adventitious carbon species from XPS measurement, while the peak at 288.9 eV can be ascribed to carbonate ion in $(BiO)_2CO_3$.[34] It is worth noting that a new peak appears at ca. 283.05 eV for the C-doped $(BiO)_2CO_3$ samples, which can be indexed to the Bi-C bond,[45] suggesting the successful incorporation of external carbon elements into the crystal structure by substituting O elements in $(BiO)_2^{2+}$ layer. This confirms the results revealed by FT-IR analysis. Moreover, the intensity of the peak at 283.05 eV increases step-by-step with the increasing carbon amount. The surface atomic concentration of the doped carbon was determined to be 0.09%, 0.13% and 0.23% for CBOC-L, CBOC-M and CBOC-H by XPS, respectively.

The DOS of the valence band is shown in Fig. 6c. The C-doped $(BiO)_2CO_3$ samples show similar valence band edge compared with the undoped $(BiO)_2CO_3$. Notably, some new localized electronic states are observed for the C-doped $(BiO)_2CO_3$ samples, which indicates that the doped carbon does not change the valence band position but creates some isolated localized states above the valence band edge. Similar phenomenon has been observed for C-doped TiO_2 photocatalyst reported by Kisch et al.[11]

3.4 Optical Property, Photocurrent Generation and Charge Separation.

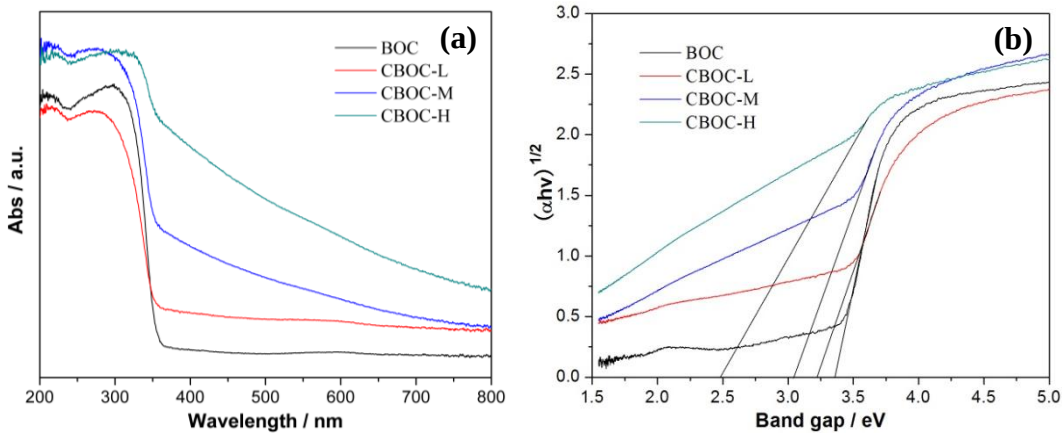

Fig. 7 UV–vis DRS (a) and plots of $(\alpha hv)^{1/2}$ vs. photon energy (b) of the as-prepared four samples.

The optical properties of $(BiO)_2CO_3$ were investigated using UV–vis DRS and the results are shown in Fig. 7. Fig. 7a shows that the undoped $(BiO)_2CO_3$ exhibits absorption in UV light region with the wavelength shorter than 360 nm. In contrast to the undoped $(BiO)_2CO_3$, the absorption edges of the C-doped $(BiO)_2CO_3$ samples are red-shifted and extend to the whole visible light region. Furthermore, the absorption edges of the samples shift monotonically to longer wavelengths as the amount of doped carbon increases, in agreement with the transformation of samples' color from white to light grey and dark grey. The tail absorption of the C-doped $(BiO)_2CO_3$ samples is associated with the localized electronic states observed by VB XPS (Fig. 6c). The bandgap energy estimated from the intercept of the tangents to the plots of $(\alpha hv)^{1/2}$ vs. photon energy is determined to be 3.38, 3.26, 3.05 and 2.49 eV for undoped $(BiO)_2CO_3$, CBOC-L, CBOC-M and CBOC-H, respectively (Fig. 7b),[46] indicating that the C element substituting for O element in the crystal structure narrows the bandgap of $(BiO)_2CO_3$.

As discussed in VB XPS (Fig. 6c), the introduction of C element into the crystal structure does not change the position of valence band except some localized electronic states exist above the valence band edge for the C-doped $(BiO)_2CO_3$ samples. In another word, the valence band edge is kept at the same position for all samples. Consequently, the bandgap narrowing of the C-doped $(BiO)_2CO_3$ samples should originate from the down-shift of conduction band. Since the conduction band of $(BiO)_2CO_3$ is mainly composed of the hybridized O 2p and Bi 6p,[43] the hybridized C 2p (substituting for O element) and Bi 6p will result in the down-shift of conduction band. The high absorption in the visible light range benefits from carbon doping. Besides, the special hierarchical structures confirmed by SEM may also contribute to the increased visible light absorption by allowing strong light reflection and scattering effects to increase the light harvesting efficiency.[26,27]

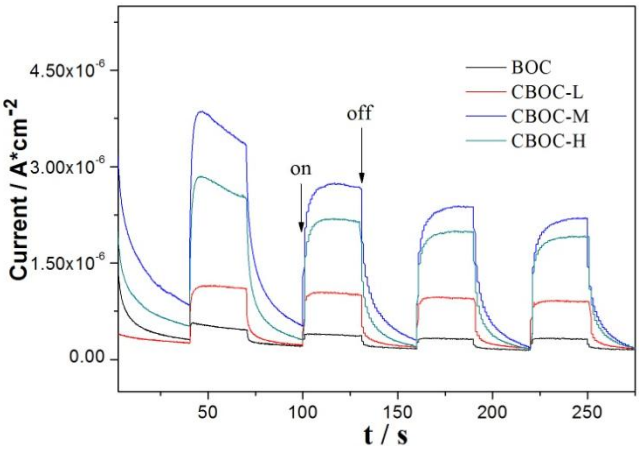

Fig. 8 Transient photocurrent density of the as-prepared samples.

Fig. 8 shows the transient photocurrent responses via four on−off cycles of the bare $(BiO)_2CO_3$ and C-doped $(BiO)_2CO_3$ samples under visible light irradiation, which directly correlate with the recombination efficiency of the photogenerated carriers.[47] The decent photocurrent density of bare $(BiO)_2CO_3$ hierarchical microspheres can be ascribed to the surface reflection and scattering effect. Obviously, the photocurrent densities of the C-doped $(BiO)_2CO_3$ are much higher than that of $(BiO)_2CO_3$, showing that the separation and transfer of photoinduced electron−hole pairs are more efficient after carbon doping. Moreover, the photocurrent intensity increases first and

then decreases with increasing carbon content and is found highest for CBOC-M. The enhanced photocurrent density induced by visible light can be ascribed to the fact that carbon doping narrows the band gap of $(BiO)_2CO_3$ and promotes the charge separation. Zhang et al. also found that C-doping can improve the efficient separation and transfer of the photogenerated electrons and holes in the C-doped $BiVO_4$ photocatalyst.[16] EIS Nyquist analysis has been conducted as shown in Fig. S3. Compared to the BOC, the impedance plot of CBOC-M exhibits a smaller radius in the dark and under visible light illumination, indicating faster interfacial electron transfer. In addition, room-temperature PL spectra for BOC and CBOC-M were conducted using the excitation light of 280 nm UV light (Fig. S4). It can be clearly seen that the PL intensity of the BOC is much higher than the CBOC-M, which confirms that carbon doping can effectively inhibit the recombination of excited electrons and holes.

Table 1 Summary of the specific surface areas, pore parameters and NO removal ratio of all the samples.

Samples	S_{BET} (m^2/g)	Total volume (cm^3/g)	Peak pore size (nm)	NO removal ratio (%)
BOC	19	0.12	22.8	18.1
CBOC-L	9	0.07	32.4	50.8
CBOC-M	13	0.09	31.6	59.7
CBOC-H	20	0.12	23.1	38.9
C-doped TiO_2[32]	122.5	0.248	2.90	20.3
N-doped $(BiO)_2CO_3$[34]	30.4	0.108	2.66	49.4

3.5 Growth mechanism and the effects of glucose.

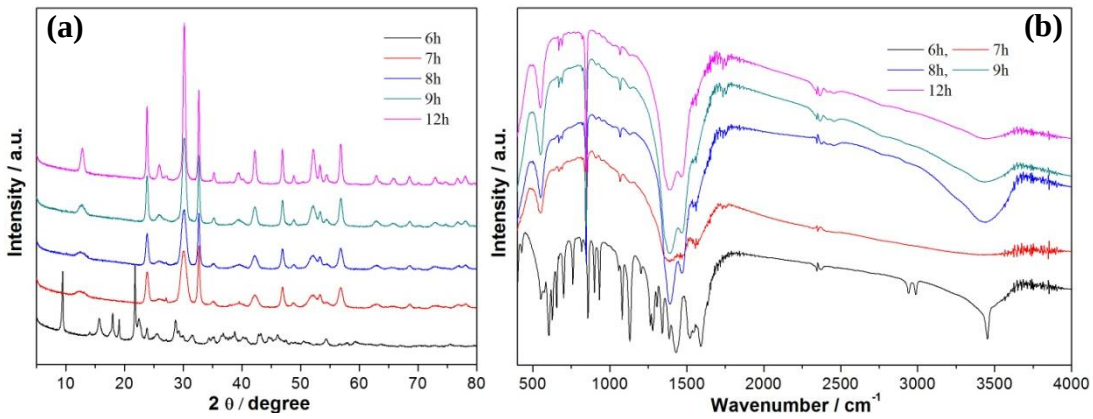

Fig. 9 XRD and FT-IR of the CBOC-M sample obtained at different reaction time.

In order to understand the evolution process of the C-doped $(BiO)_2CO_3$ samples, we carried out the time-dependent experiments of CBOC-M, during which the intermediates were collected for further analysis at different reaction stages. Fig. 9a shows the XRD patterns of the samples obtained at different reaction times between 6 to 12 h. When the reaction time reaches 6 h, the diffraction peaks of bismuth citrate still exist. Upon increasing the reaction time to 7 h, diffraction peaks of $(BiO)_2CO_3$ (JCPDS-ICDD card no. 25-1464) appear, which suggests that the chemical reaction mainly happens between 6 and 7 h. Namely, $(BiO)_2CO_3$ are generated at this stage, accompanying by the doping of carbon element into $(BiO)_2CO_3$. By prolonging the reaction time to 9 and 12 h, no new peak appears except that the diffraction intensity gradually increases, implying that the crystallinity of the samples is increased. Fig. 9b shows the FT-IR spectra of the samples prepared at different reaction times between 6 to 12 h. The FT-IR spectra of the sample obtained after 6h hydrothermal treatment are similar to bismuth citrate, which is in line with the XRD result. After reaction for more than 7 h, the internal vibrations of CO_3^{2-} ion (point group symmetry D3h) appear,[42] including symmetric stretching mode v_1 (1070 cm^{-1}), the anti-symmetric vibration v_3 (1468 and 1390 cm^{-1}), the out-of-plane bending mode v_2 (849 and 820 cm^{-1}), the in-plane deformation v_4 (694 and 675 cm^{-1}), and v_1+v_4 (1755 and 1729 cm^{-1}). Later, some peak positions experience a slight shift with the increased reaction time, which can be ascribed to the variation of chemical environment of the bonds during structural evolution.

Based on these observation, we can conclude that the introduction of glucose into the reaction system prolongs the initial stage of the hydrolysis of bismuth citrate but accelerates the generation of $(BiO)_2CO_3$ in comparison with the reaction system without glucose as reported in our previous work.[43] The effects of glucose on the

chemical reaction are proposed as follows. Initially, patial glucose is decomposed to yield CO_3^{2-} (reaction (1)), which inhibits the hydrolysis of Na_2CO_3 (reaction (2)). Thus, the hydrolysis of bismuth citrate by OH^- is delayed (reaction (3)). However, some OH^- still exist in the aqueous solution. With the increasing time, Bismuth citrate can be hydrolyzed by OH^-. The aqueous solution contains large amount of CO_3^{2-} ions, which come from both the glucose and Na_2CO_3. These CO_3^{2-} ions can take part in reaction (4) and (5). Thus, the additive glucose could accelerate the reaction progress and shorten the reaction time. In additon, partial glucose is carbonized into hydrophilic carbon colloid during hydrothermal treatment,[15] which can be in situ embedded in the matrix of $(BiO)_2CO_3$ as the carbon doping source. As shown in the Fig S1, $(BiO)_2CO_3$ has a Sillen layered structure. It consists of $[Bi_2O_2]^{2+}$ layers intercalated by CO_3^{2-} groups, and weak van der Waals interactions exist among the layers. According to FT-IR analysis, C atoms was not incorporated into the CO_3^{2-} group. Also, XPS analysis revealed that the peak belonging to Bi-C bonds are observed for the C-doped $(BiO)_2CO_3$ samples, suggesting the successful incorporation of external carbon elements into the crystal structure by substituting O elements in $(BiO)_2^{2+}$ layer. Consequently, it is concluded that the C element substituted the O elements in $(BiO)_2^{2+}$ layer.

$$C_6H_{12}O_6 \text{ (glucose)} \rightarrow CO_2 + H_2O \rightarrow CO_3^{2-} + 2H^+ \quad (1)$$

$$Na_2CO_3 + 2H_2O \rightarrow CO_3^{2-} + 2OH^- + 2Na^+ + 2H^+ \quad (2)$$

$$Bi^+ \text{ (citrate)} + 3OH^- \rightarrow BiO^+ + \text{citrate} + 3H^+ \quad (3)$$

$$4BiO^+ + CO_3^{2-} + 2OH^- \rightarrow (BiO)_4CO_3(OH)_2 \text{ (s)} \quad (4)$$

$$(BiO)_4CO_3(OH)_2\text{(s)} + CO_3^{2-} \rightarrow 2(BiO)_2CO_3\text{(s)} + 2OH^- \quad (5)$$

3.6 Photocatalytic Activity, Mechanism and Photochemical Stability.

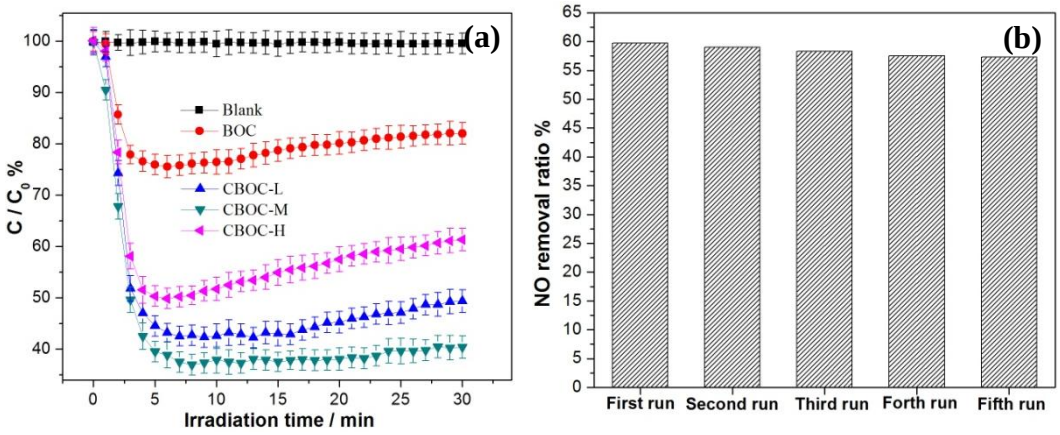

Fig. 10 Photocatalytic NO removal performance of the as-prepared samples under visible light irradiation (a) and the cycle photocatalytic activity of CBOC-M sample (b).

The photocatalytic NO removal performance of the samples was evaluated in the air under visible light irradiation (λ>420nm). As presented in Fig. 10a, NO cannot be removed without photocatalysts under visible light irradiation. In the presence of BOC, 18.1% removal ratio is achieved after 30 min irradiation, which is attributed to the extrinsic absorption of BOC due to the hierarchical structure demonstrated by our previous study.[27] The removal ratio of CBOC-L sample increases to 50.8% when introducing small amount of external C element in the crystal structure. With an increase in C concentration, an admirable high photocatalytic activity with a NO removal ratio of 59.7% can be observed for CBOC-M, which is much higher than BOC, C-doped TiO_2[32] and N-doped $(BiO)_2CO_3$ hierarchical microspheres[34]. Then, the photocatalytic activity of C-doped $(BiO)_2CO_3$ decreases with increased carbon content. CBOC-H displays a removal ratio of 38.9%. The photocatalytic activity increases first and then decreases, which is consistent with the photocurrent efficiency. Higher carbon content is likely to form more defect sites in the lattice, which probably act as recombination centers.[48] Thus, the CBOC-H shows decreased photocurrent response and photocatalytic activity. This result suggests that there exists an optimal amount of doping carbon in the $(BiO)_2CO_3$ to improve the photocatalytic activity of $(BiO)_2CO_3$. Moreover, the reaction rate constant *k* of BOC, CBOC-L, CBOC-M and CBOC-H is determined to be 0.078, 0.214, 0.231 and 0.185 min^{-1}, respectively (Fig. S5). The apparent quantum efficiency was also estimated to be 16.3, 45.5, 49.1 and 39.3% for BOC, CBOC-L, CBOC-M and CBOC-H, respectively (Details about apparent quantum efficiency calculations are given in SI). Obviously, the C-doped $(BiO)_2CO_3$ samples exhibit higher reaction rate constant *k* and apparent quantum efficiency than BOC. Aiming to examine the photocatalytic stability of CBOC-M, the circulating runs in the photocatalytic removal of NO under visible light irradiation are performed. As shown in Fig. 10b, the CBOC-M sample still maintains relatively stable photocatalytic activity with no obvious deactivation after five repetitive cycles. The reproducibility and stability are improtant to photocatalysts for potential

applications.[49-51] To survey the reproducibility of the photocatalysts, we have repeatedly prepared CBOC-M by the same method, and investigated its photocatalytic performance. From Fig. S6, the CBOC-M photocatalyst exhibits almost the same visible photocatalytic activity with the pristine CBOC-M obtained for the first time. In addition, the SEM, XRD, FT-IR spectra and UV-vis DRS of CBOC-M after photocatalytic reaction were performed to investegate its stability as shown in Fig. S7. XRD combined with SEM analysis of CBOC-M show that the crystal structure and morphology of the photocatalyst were not altered after the photocatalytic reaction. FT-IR spectra and UV-vis DRS are the same as those of the fresh sample. These results imply the excellent stability and reproducibility of the C-doped $(BiO)_2CO_3$ hierarchical self-assembly as visible light photocatalysts.

In the case of CBOC-L and CBOC-M, the bandgap are too large to be excited by visible light, but the electrons in the localized electronic states can be excited by visible light to the conduction band. While for CBOC-H, the electrons in both the valence band and localized states can be excited to the conduction band. As demonstrated by our previous report, the photogenerated holes and OH are found to be the main active species for $(BiO)_2CO_3$ to remove NO.[27] Here, similarly, the holes in the valence band or/and localized states after photoexcitation can be directly involved in the photocatalytic reaction or generate OH by reacting with surface adsorbed water/hydroxyl groups. In accordance with the results above, a schematic band structure is proposed for the undoped and C-doped $(BiO)_2CO_3$ samples as shown in Fig. 11.

Carbon doping could reduce the band gap of $(BiO)_2CO_3$, and generate localized states above the valence band, resulting in extending the light response to visible region. On the other hand, carbon doping promotes the effective separation of photogenerated charge carriers. As a result, C-doped $(BiO)_2CO_3$ samples exhibited enhanced visible photocatalytic activity in comparison with the undoped $(BiO)_2CO_3$. When compared with the C-doped TiO_2 (20.3%), the C-doped $(BiO)_2CO_3$ exhibited superior photocatalytic activity as well, which can be attributed to the assembled hierarchical structure. Multiple scattering and reflection of incident light are allowed in the hierarchical structure, which consequently increase the quantity of photoinduced electrons and holes to initial the photocatalytic reaction. Also, the hierarchical structure benefits the diffusion of reaction intermediates and products to accelerate the reaction rate. As reported by Kisch et al, C-doped TiO_2 was found to be more active than N-doped TiO_2.[11] Here, the C-doped $(BiO)_2CO_3$ (CBOC-M) also exhibits more efficient visible photocatalytic activity than the N-doped $(BiO)_2CO_3$ (49.4%) mainly because of the stronger visible light absorption of CBOC-M. In a word, the modified band structure, improved separation efficiency of photo-induced carriers as well as the special hierarchical structure could make C-doped $(BiO)_2CO_3$ hierarchical self-assembly with outstanding visible light photocatalytic activity.

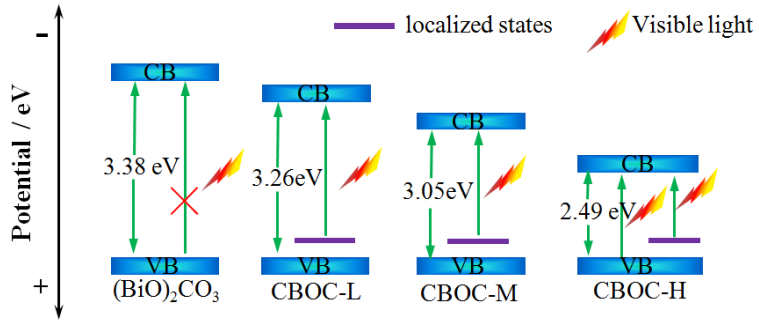

Fig. 11 Proposed schematic energy band structure of the as-prepared samples.

In order to investigate the influence of carbon source on the doped $(BiO)_2CO_3$ samples. We employed other carbohydrates such as maltose, fructose, sucrose and starch as carbon doping source to prepare C-doped $(BiO)_2CO_3$, while keeping the synthesis conditions identical with CBOC-M. As expected, our preliminary results indicate that the C-doped $(BiO)_2CO_3$ samples prepared from different carbon sources could also exhibit a red-shift in absorption edges and show enhanced visible light absorption (Fig. S8). These photocatalysts are expected to exhibit high visible photocatalytic activity. Therefore, this green synthetic route could provide a general green approach to fabricate efficient visible light photocatalysts involved with in situ carbon doping. We believe that it is significant to develop such an energy-saving and environmentally benign method to achieve effective environmental catalysts as it is efficient in scale-up and benign to the environment.

4. Conclusion

In summary, we have developed a facile one-pot synthetic route for C-doped $(BiO)_2CO_3$ hierarchical self-assembly using glucose as carbon source for the first time. The doped carbon element could narrow the band gap via down-shifting the conduction band, and simultaneously created some localized states above the valence band edge. Incorporation of external carbon element into the lattice not only increased the visible light absorption, but also improved the efficient separation and transfer of the photogenerated electrons and holes. At the same time, the hierarchical structures enhanced the light-harvesting and utilization and contributed to the diffusion of reaction

intermediates and products. Consequently, the as-prepared C-doped $(BiO)_2CO_3$ hierarchical microspheres exhibited enhanced visible photocatalytic activity toward the removal of NO in comparison with the undoped $(BiO)_2CO_3$, C-doped TiO_2 and N-doped $(BiO)_2CO_3$. Furthermore, the good photocatalytic activity of the as-prepared C-doped $(BiO)_2CO_3$ photocatalysts were demonstrated to be stable and reproducible. The growth mechanism of C-doped $(BiO)_2CO_3$ hierarchical self-assembly has been proposed. The introduction of glucose into the hydrothermal reaction prolongs the initial stage of the hydrolysis of bismuth citrate and accelerates the generation of $(BiO)_2CO_3$ crystals. Other carbohydrates such as maltose, fructose, sucrose and starch can also be used as carbon source to synthesize C-doped $(BiO)_2CO_3$, which demonstrate the generality of the present method. It is of great importance to provide a simple and general method to develop highly active C-doped $(BiO)_2CO_3$ photocatalysts with both carbon doping and structural optimization. This perspective could also serve as an effective route for tailoring the optical properties and photocatalytic activity of other wide band gap semiconductors.

Acknowledgments

This research is financially supported by the National Natural Science Foundation of China (51478070, 51108487), the Science and Technology Project from Chongqing Education Commission (KJ1400617), and the Innovation Project for Postgraduates from Chongqing Education Commission (CYS14172).

Notes and references

1 C. C. Chen, W. H. Ma and J. C. Zhao, *Chem. Soc. Rev.* 2010, **39**, 4206−4219.
2 H. Xu, S. Ouyang, L. Liu, P. Reunchan, N. Umezawa and J. Ye, *J. Mater. Chem. A*, 2014, **2**, 12642−12661
3 S. W. Cao and J. G. Yu, *J. Phys. Chem. Lett.* 2014, **5**, 2101−2107.
4 F. Fresno, R. Portela, S. Suárez and J. M. Coronado, *J. Mater. Chem. A*, 2014, **2**, 2863−2884.
5 Z. Zhao, Y. Sun and F. Dong, *Nanoscale*, 2015, **7**, 15−37.
6 F. Dong, Z.Y. Wang, Y.H. Li, W.K. Ho and S.C. Lee, *Environ. Sci. Technol.*, 2014, **48**, 10345−10353.
7 K. Zhang, J. Liang, S. Wang, J. Liu, K. Ren, X. Zheng, H. Luo, Y. Peng, X. Zou, X. Bo, J. Li and X. Yu, *Cryst. Growth Des*. 2012, **12**, 793−803.
8 Y. Hong, C. Tian, B. Jiang, A. Wu, Q. Zhang, G. Tian and H. Fu, *J. Mater. Chem. A*, 2013, **1**, 5700−5708.
9 V. Etacheri, R. Roshan and V. Kumar, *ACS Appl. Mater. Interfaces* 2012, **4**, 2717–2725.
10 G. Jiang, R. Wang, X. Wang, X. Xi, R. Hu, Y. Zhou, S. Wang, T. Wang and W. Chen, *ACS Appl. Mater. Interfaces* 2012, **4**, 4440–4444.
11 F. Dong, Q. Y. Li, Y. J. Sun and W. K. Ho, *ACS Catal.*, 2014, **4**, 4341−4350.
12 G. Yang, Z. Jiang, H. Shi, T. Xiao and Z. Yan, *J. Mater. Chem*., 2010, **20**, 5301–5309.
13 A. Gasparotto, D. Barreca, D. Bekermann, A. Devi, R. A. Fischer, P. Fornasiero, V. Gombac, O. I. Lebedev, C. Maccato, T. Montini, G. V. Tendeloo and E. Tondello, *J. Am. Chem. Soc*. 2011, **133**, 19362–19365.
14 Y. Park, W. Kim, H. Park, T. Tachikawa, T. Majima and W. Choi, *Appl. Catal. B-Environ.*, 2009, **91**, 355–361.
15 F. Dong, H. Wang and Z. Wu, *J. Phys. Chem. C*, 2009, **113**,16717–16723.
16 C. Yin, S. Zhu, Z. Chen, W. Zhang, J. Gu and D Zhang, *J. Mater. Chem. A*, 2013, **1**, 8367−8378.
17 M. Zhou, X. Gao, Y. Hua, J. Chen and X. Hu, *Appl. Catal. B-Environ.*, 2013, **138–139**, 1–8.
18 H. B. Wu, J. S. Chen, X. W. Lou and H. H. Hng. *J. Phys. Chem. C*, 2011, **115**, 24605–24610.
19 H. Y. Chen, D. B. Kuang and C. Y. Su, *J. Mater. Chem.*, 2012, **22**,15475–15489..
20 C. M. A. Parlett, K. Wilson and A. F. Lee, *Chem. Soc. Rev.*, 2013, **42**, 3876–3893.
21 L. Chen, J. He, Q. Yuan, Y. Liu, C.-T. Au and S.-F. Yin, *J. Mater. Chem. A*, 2015, **3**, 1096−1102.
22 L. Zhang, W. Wang, Z. Chen, L. Zhou, H. Xu and W. Zhu, *J. Mater. Chem.*, 2007, **17**, 2526–2532.
23 Y. Lei, G. Wang, S. Song, W. Fan, M. Pang, J. Tang and H. Zhang, *Dalton Trans.*, 2010, **39**, 3273–3278.
24 F. Dong, W.-K. Ho, S. C. Lee, Z. Wu, M. Fu, S. Zou and Y. Huang, *J. Mater. Chem.*, 2011, **21**, 12428–12436.
25 J. Y. Xiong, Z. B. Jiao, G. X. Lu, W. Ren, J. H. Ye and Y. P. Bi, *Chem. Eur. J.*, 2013, **19**, 9472–9475.
26 Z. L. He and W. X. Que, *Phys. Chem. Chem. Phys.*, 2013, **15**, 16768−16773.
27 T. Xiong, F. Dong and Z. Wu, *RSC Adv.*,2014, **4**, 56307–56312.
28 G. Cheng, H. M. Yang, K. F. Rong, Z. Lu, X. L. Yu and R. Chen, *J. Solid State Chem.*, 2010, **183**, 1878–1883.
29 Y. Zhou, H. Y. Wang, M. Sheng, Q. Zhang, Z. Y. Zhao, Y. H. Lin, H. F. Liu and G. R. Patzke, *Sens. Actuators, B-Chemical*, 2013, **188**, 1312−1318.
30 S. Peng, L. Li, H. Tan, Y. Wu, R. Cai, H. Yu, X. Huang, P. Zhu, S. Ramakrishna, M. Srinivasan and Q. Yan, *J. Mater. Chem.* A, 2013, **1**, 7630−7638.
31 P. Madhusudan, J. Zhang, B. Cheng and G. Liu, *CrystEngComm*, 2013, **15**, 231−240.
32 F. Dong, S. C. Lee, Z. Wu, Y. Huang, M. Fu, W. K. Ho, S. Zou and B. Wang, *J. Hazard. Mater.*, 2011, **195**, 346–354.
33 L. Chen, R. Huang, S. F. Yin, S. L. Luo and C. T. Au, *Chem. Eng. J.*, 2012, **193-194**, 123−130
34 F. Dong, H. T. Liu, W. K. Ho, M. Fu and Z. B. Wu, *Chem. Eng. J.*, 2013, **214**, 198−207.

35 F. Dong, T. Xiong, R. Wang, Y. J. Sun and Y. K. Jiang, *Dalton Trans.*, 2014, **43**, 6631–6642.
36 F. Dong, Q. Y. Li, Y. Zhou, Y. J. Sun, H. D. Zhang and Z. B. Wu, *Dalton Trans.* 2014, **43**, 9468–9480.
37 L. Chen, S.-F. Yin, S.-L. Luo, R. Huang, Q. Zhang, T. Hong and P. C. T. Au, *Ind. Eng. Chem. Res*. 2012, **51**, 6760−6768
38 N. Liang, M. Wang, L. Jin, S. Huang, W. Chen, M. Xu, Q. He, J. Zai, N, Fang and X. Qian, *ACS Appl. Mater. Interfaces* 2014, **6**, 11698−11705.
39 N. Liang, J. Zai, M. Xu, Q. Zhu, X. Wei and X. Qian, *J. Mater. Chem. A.*, 2014**, 2**, 4208–4216.
40 W. D. Zhang, Y. J. Sun, F. Dong, W. Zhang, S. Duan and Q. Zhang, *Dalton Trans.*, 2014, **43**, 12026–12036.
41 M. Xiong, L. Chen, Q. Yuan, J. He, S. L. Luo, C. T. Au and S. F. Yin, *Dalton Trans*., 2014, **43**, 8331−8337.
42 G. E. Tobon-Zapata, S. B. Etcheverry and E. J. Baran, *J. Mater. Sci. Lett*., 1997, **16**, 656–657.
43 F. Dong, A. M. Zheng, Y. J. Sun, M. Fu, B. Q. Jiang, W. K. Ho, S. C. Lee and Z. B. Wu, *CrystEngComm*, 2012, **14**, 3534–3544.
44 K. S. W. Sing, D. H. Everett, R. A. W. Haul, L. Moscou, R. A. Pierotti, J. Rouquerol and T. Siemieniewska, *Pure Appl. Chem.*, 1985, **57**, 603–619.
45 J. H. Yu, B. Wei, L. Zhu, H. Gao, W. J. Sun and L. L. Xu, *Appl. Surf. Sci.* 2013, **284**, 497–502.
46 M. A. Butler, *J. Appl. Phys*., 1977, **48**, 1914–1920.
47 H. Park and W. Choi, *J. Phys. Chem. B*, 2003, **107**, 3885−3890.
48 H. Irie, Y. Watanabe and K. Hashimoto, *J. Phys. Chem. B*, 2003, **107**, 5483–5486.
49 H. Lv, J. Song, Y. V. Geletii, J. W. Vickers, J. M. Sumliner, D. G. Musaev, P. Kögerler, P. F. Zhuk, J. Bacsa, G. Zhu and C. L. Hill, *J. Am. Chem. Soc.*, 2014, **136**, 9268–9271,
50 F. Song, Y. Ding, B. Ma,C. Wang, Q. Wang, X. Du, S. Fu and J. Song, *Energy Environ. Sci.*, 2013, **6**, 1170–1184 .
51 J. Song, Z. Luo, D. K. Britt, H. Furukawa, O. M. Yaghi, K. I. Hardcastle and C. L. Hill, *J. Am. Chem. Soc.*, 2011, **133**, 16839–16846.